Electronic structure and excitonic absorption in BaCu*Ch*F (*Ch*=S, Se, and Te)

A. Zakutayev,* R. Kykyneshi, G. Schneider, D. H. McIntyre, and J. Tate†
Department of Physics, Oregon State University, Corvallis, Oregon 97331, USA
(Received 29 December 2009; revised manuscript received 9 March 2010; published 2 April 2010)

Double excitonic absorption peaks are observed in textured BaCuSF and BaCuSeF thin films. The excitonic doublet separation increases with increasing fraction of heavy chalcogen in the thin-film solid solutions, in good agreement with the spin-orbit splitting of the valence bands calculated by density-functional theory. In BaCuSF and BaCuSeF, the excitons have large binding energies (95 and 65 meV, respectively) and can be observed at room temperature. A three-dimensional Wannier-Mott excitonic absorption model gives good agreement between the experimental and theoretical optical properties. Band gaps of BaCuSF and BaCuSeF calculated using the GW approximation agree with experiment. In BaCuTeF, transitions across the lowest direct energy gap and excitonic absorption are suppressed, extending its transparent range.

DOI: 10.1103/PhysRevB.81.155103 PACS number(s): 71.35.Cc, 71.70.Ej, 71.20.Nr, 78.66.−w

I. INTRODUCTION

Quaternary mixed-anion compounds with the ZrCuSiAs-type layered crystal structure (P4/*nmm* space group), such as oxychalcogenides,[1] fluorochalcogenides,[2] and oxypnictides[3] have recently received considerable attention. The large number of possible combinations of components and dopants results in interesting physical properties such as simultaneous transparency and degenerate *p*-type conductivity,[4] ferromagnetic response,[5] and high-temperature superconductivity.[6] These materials have potential applications in different technological fields such as transparent electronics,[7] thermoelectrics,[8] optoelectronics,[9] and photovoltaics.[10]

In this paper, we present a detailed experimental and theoretical study of the electronic and optical properties of one family in this group, Ba-based chalcogenide-fluorides BaCu*Ch*F (*Ch*=S,Se,Te) and their solid solutions, which show *p*-type conductivity, wide direct optical band gaps, and room temperature excitons. The structural anisotropy of BaCu*Ch*F gives rise to anisotropic effective masses of electrons and holes, and to large exciton reduced masses ($0.90m_e$ and $0.80m_e$ in BaCuSF and BaCuSeF respectively, compared to $0.058m_e$ in GaAs), which lead to large exciton binding energies (95 meV and 65 meV, compared to 4.2 meV in GaAs).[11] Spin-orbit coupling in the *Ch* atom results in degeneracy removal at the Γ point of the BaCu*Ch*F valence band, which in turn causes splitting of the excitonic absorption peaks. The peak splitting can be tuned by changing the chalcogen content of BaCu*Ch*F-based thin-film solid solutions. BaCuTeF thin films exhibit no excitonic absorption because the electron-hole interaction is screened by a high concentration of free holes that also cause a moderate valence band filling effect. The transparency range of thin-film BaCuTeF is comparable to that of BaCuSeF, the major reason being suppressed interband transitions.

The BaCu*Ch*F materials are similar to their isostructural counterparts, the La-based layered oxychalcogenides where the $[Ba_2^{2+}F_2^{1-}]^{2+}$ sheets are replaced by $[La_2^{3+}O_2^{2-}]^{2+}$ layers.[12] LaCuO*Ch* and their solid state solutions also have spin-orbit split excitonic peaks followed at higher energies by stepwise absorption spectra with lower-intensity peaks.[13] The separation between the excitonic absorption peaks increases with increasing atomic weight of *Ch* (S or Se) or Ln (La, Pr or Nd) in the solid solutions, which is attributed to spin-orbit coupling effects.[14] The exciton binding energy in LaCuOS and LaCuOSe (50 meV)[15] is smaller than in BaCuSF and BaCuSeF. While LaCuOTe develops an indirect band gap,[16] BaCuTeF retains a direct band gap at the Γ-point.

The experimental and computational details are followed by a description of the BaCu*Ch*F electronic structure and optical properties. The discussion is divided into three subsections. First, we consider BaCuSF and BaCuSeF, analyzing the exciton absorption in terms of a three-dimensional (3D) Wannier-Mott model. Second, we consider BaCuTeF, its higher-than-expected transparency, and the absence of excitonic absorption. Finally, we discuss the absorption spectra of the BaCu($Ch_{1-x}Ch'_x$)F thin-films solid solutions.

II. EXPERIMENTAL AND COMPUTATIONAL METHODS

Thin films of BaCu*Ch*F (*Ch*=S,Se,Te) were deposited by pulsed laser deposition (PLD) from dense, single-phase ceramic targets, and BaCu($Ch_{1-x}Ch'_x$)F thin-film solid solutions were prepared by alternating PLD from these targets. All the films were phase pure, of excellent quality and highly *c*-axis oriented. BaCuSeF and BaCuTeF films also exhibited strong in-plane order. The concentration of free holes in these samples was determined using Hall effect measurements to be 10^{19} and 10^{20} cm^{-3} respectively, in close agreement with the results in Refs. 17 and 18. For BaCuSF, the carrier concentration could not be reliably measured using this method, but it was estimated to be 10^{18} cm^{-3} based on the measurement of the resistivity and on the calculation of the effective mass of the holes. More details of the preparation and characterization are described elsewhere.[18] The experimental thin film absorption spectra were determined from the transmittance and reflectance spectra, measured between 300 and 80 K, using an analysis that removes the thin-film interference fringes that appear in the raw data in the region of the spectrum where the films are transparent.[19]

Most of the density-functional theory (DFT) calculations were carried out with the Wien[20] and Flair[21] codes that use

the full-potential linearized augmented plane-wave formalism within the Perdew-Burke-Ernzerhof generalized gradient approximation (GGA) of DFT. The muffin-tin radii were set to 2.5 a.u. for Ba and Cu in all BaCu*Ch*F, 2.2 a.u. and 2.3 a.u. for S and F in BaCuSF, 2.3 a.u. and 2.4 a.u. for Se and F in BaCuSeF, and 2.5 a.u. and 2.5 a.u. for Te and F in BaCuTeF, respectively. The potentials and charge densities were expanded on a k-mesh of 6875 points in the Brillouin zone, including 546 unique k points. Inside the muffin-tin spheres, the potentials and charge densities were expanded up to $l=10$, while in the interstitial regions, they were expanded using 3523 plane waves. The calculations were iterated until the total energies converged to better than 0.1 mRy and the total charge converged to better than $10^{-3}e$. GGA DFT results were used as input for the electronic band structure calculation that included many-body effects in the GW approximation[22] and is referred to as the "GW calculation" in the text. The GW calculation was performed with the VASP[23] code using the projector-augmented-wave method was used with a $6\times6\times3$ k-point mesh, and a 275 eV plane-wave cutoff energy. The GW calculation gives a realistic band gap estimate, but it is computationally expensive, so we used GGA DFT as described above for the spin-orbit effects, absorption spectra, and effective mass calculations.

III. RESULTS

A. Electronic structure

The GGA DFT results reported here extend our previously reported calculations,[24] which indicated that the valence bands (VB) of BaCu*Ch*F are degenerate at the Γ point. Spin-orbit interaction effects included in the present calculation remove this degeneracy [Fig. 1(a)]. The separation between spin-orbit split bands A and B (VB_A and VB_B) Δ_{SO} increases from BaCuSF (22 meV) through BaCuSeF (89 meV) to BaCuTeF (250 meV). The valence band maximum (VBM) of BaCu*Ch*F is highly anisotropic as a consequence of the layered crystal structure. The valence bands are narrow in the ΓZ direction, which corresponds to the crystallographic c axis in the tetragonal crystal structure, but broad in the ΓX direction, which lies in the ab plane of the crystal.

All three members of BaCu*Ch*F family have similar band character near the valence band maximum (VBM) [Fig. 1(b)]. The VBM is composed of Cu 3d orbitals well mixed with *Ch* np orbitals ($n=3$ for S, $n=4$ for Se and $n=5$ for Te). As the mass of the *Ch* atom increases, the ratio of *Ch* np to Cu 3d character at the VBM also increases. This can be explained by the upward shift of the *Ch* np level. The bands derived from fluorine (F) atomic orbitals lie deeper and have almost no contribution to either the VBM or the conduction band minimum (CBM).

In contrast to the VB, the conduction band (CB) character of BaCuTeF is significantly different from that of BaCuSF and BaCuSeF, as shown in Fig. 1. In BaCuSF (BaCuSeF), two lowest conduction bands (CB_I and CB_{II}) are composed of Cu 4s and Ba 5s atomic orbitals well hybridized with S 3s (Se 4s) states, but in BaCuTeF, the corresponding band appears as the fourth conduction band (CB_{IV}). The third conduction band (CB_{III}) in BaCuSF and BaCuSeF is derived

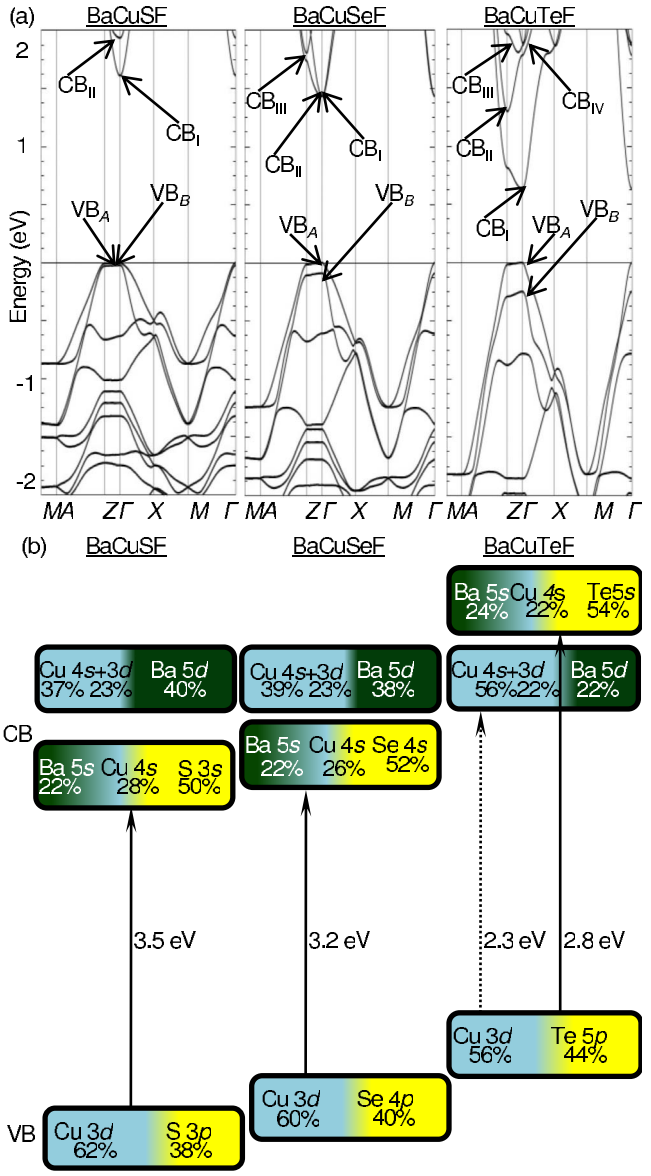

FIG. 1. (Color online) (a) Relativistic band structure of BaCu*Ch*F calculated by GGA DFT. The spin-orbit split valence bands are labeled VB_A and VB_B, while the conduction bands are labeled CB_I, CB_{II}, CB_{III}, and CB_{IV}. (b) Schematic electronic structure of BaCu*Ch*F compounds. The band gaps in (b) are calculated using the GW approximation.

from Cu 4s and Cu 3d atomic orbitals mixed with Ba 5d levels and is similar in character to the lowest conduction band (CB_I) in BaCuTeF. CB_{II} and CB_{III} in BaCuTeF are also derived mostly from Cu and Ba states.

The GGA DFT directional effective masses of the holes and electrons, their ratios and averages are summarized in Table I. The in-plane effective mass of the holes m_x^{VB} is significantly smaller than their out-of-plane effective mass m_z^{VB}, so the anisotropy m_z^{VB}/m_x^{VB} is large. The hole effective masses decrease with increasing atomic mass of the chalcogen in BaCu*Ch*F. The effective masses of the electrons in BaCuSF and BaCuSeF are more isotropic, as expected from the s-character of CB_I. This is not the case for BaCuTeF due to the contribution from directional d states to

TABLE I. Effective masses in BaCu*Ch*F calculated by GGA DFT. m_{av} is weighted average (2:1) of m_x and m_z. The band designations are those in Fig. 1.

Effective mass (m_e)	BaCuSF		BaCuSeF		BaCuTeF	
	CB_I	VB_A	CB_I	VB_A	CB_I	VB_A
m_x	0.68	5.41	0.54	4.23	0.51	3.85
m_z	0.92	37.5	0.82	34.7	2.94	27.0
m_{av}	0.76	16.1	0.63	14.4	1.32	11.6
m_z/m_x	1.35	6.92	1.53	8.21	5.81	7.01

CB_I. The average effective masses of the electrons and holes ($m^{CB}{}_{av}$ and $m^{VB}{}_{av}$) were obtained from a weighted average (2:1) of the in-plane and out-of-plane effective masses (Table I).

Band gaps of BaCu*Ch*F compounds calculated by GGA DFT and GW are summarized in Table II. The "electronic" band gap refers to the energy difference between the VBM and CBM and the "optical" band gap refers to the energy where the calculated absorption coefficient begins to increase significantly. We note that: (i) GGA DFT underestimates the band gaps compared to GW calculations; (ii) according to both calculations, the electronic band gap decreases from BaCuSF to BaCuSeF to BaCuTeF, and (iii) both calculations agree that the electronic and optical band gap are the same in BaCu*Ch*F (*Ch*=S,Se), and that optical band gap is larger than electronic in BaCuTeF.

B. Optical properties

Figure 2(a) shows experimental room-temperature absorption spectra with the GW electronic gaps indicated by arrows. The main features of Fig. 2(a) are following. (i) There are narrow near-band-edge absorption peaks in the spectra of BaCuSF and BaCuSeF thin films, and these peaks are absent from the BaCuTeF absorption spectrum. (ii) The spectral position of the peaks is below the GW electronic band gap prediction for BaCuSF and BaCuSeF. (iii) The energy of the strong absorption edge in BaCuTeF thin films is similar to that in BaCuSeF and much higher than the BaCuTeF electronic gap calculated by GW. Table III and Fig. 2(b) summarize the positions of strong absorption edges from Fig. 2(a). Figure 2(b) also includes similar information for BaCu($Ch_{1-x}Ch'_x$)F films and powders (the latter from diffuse reflection measurements). The absorption edge in BaCu*Ch*F films is at higher energies than in BaCu*Ch*F powders, and this difference is the most dramatic in BaCuTeF. Figure 2(c) shows the theoretical GGA DFT optical absorption spectra, with the GGA DFT electronic gaps indicated by arrows. The BaCuSF and BaCuSeF absorption edges are close to the energy of the electronic gaps, while for BaCuTeF, the absorption edge is significantly higher.

Figure 3 presents experimental optical absorption spectra of (a) BaCuSF, (b) BaCuSeF and (c) BaCuTeF thin films from 80 K to 250 K. At the lowest accessible temperature (80 K), two excitonic peaks are clearly distinct in BaCuSeF and are labeled A_1 and B_1. In addition, there is a weak shoulder on the high-energy side of each peak, and these shoulders are labeled A_2 and B_2, respectively. In the 80-K BaCuSF spectrum in Fig. 3(a), A and B are closer together and there is a step in the absorption spectrum close to 3.8 eV. The A and B absorptions broaden as the temperature increases, and persist to 400 K, the highest temperature attainable in the experimental setup. The BaCuTeF absorption spectra in Fig. 3(c) show no excitonic peaks even at 80 K, but instead there are two weakly temperature dependent absorption edges, labeled α and β. The separation of A and B and of α and β at 80 K are larger by about 30 meV, than the calculated spin-orbit splitting of the corresponding VBM. Figure 4 shows experimental absorption spectra of BaCu($S_{1-x}Se_x$)F and BaCu($Se_{1-x}Te_x$)F thin-film solid solutions. The excitonic absorption peaks of the mixed-chalcogen films are broader than those of the single-chalcogen samples. In general, as x increases, there is a gradual shift of the excitonic peaks to lower energy, an increase in peak separation, and a decrease of intensity when Te is added to the thin-film solid solution.

IV. DISCUSSION

A. BaCuSF and BaCuSeF

We attribute the A and B peaks in the experimental absorption spectra [Fig. 2(a)] of BaCuSF and BaCuSeF thin films to excitonic absorption. The peaks are absent from the

TABLE II. Theoretical electronic and optical band gaps in BaCu*Ch*F. The GW optical band gap for BaCuTeF is the difference between the VB and CB_{IV}.

Band gap (eV)	BaCuSF		BaCuSeF		BaCuTeF	
	Electronic	Optical	Electronic	Optical	Electronic	Optical
GGA DFT	1.63	1.63	1.49	1.49	1.02	1.49
GW	3.72	3.72	3.27	3.27	2.11	3.05

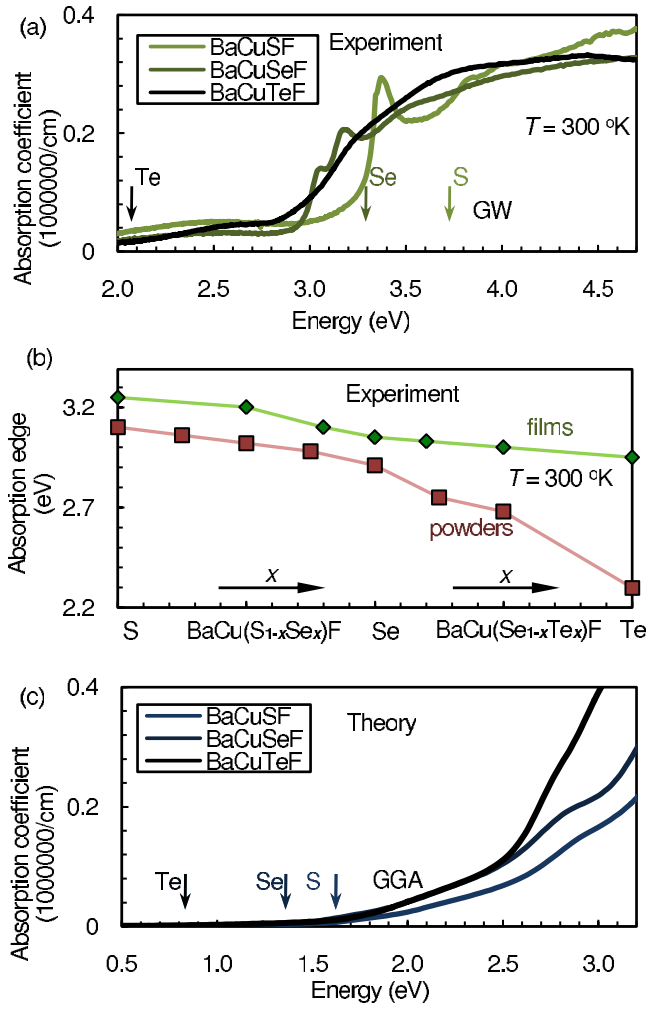

FIG. 2. (Color online) (a) Room-temperature experimental absorption spectra of BaCu*Ch*F. (b) Experimental absorption edge of BaCu($Ch_{1-x}Ch'_x$)F thin films (diamonds) and powders (squares). The lines are guides to the eye. (c) Theoretical absorption spectra of BaCuSF, BaCuSeF and BaCuTeF. The arrows in (a) and (c) indicate the electronic band gap as estimated by GW and GGA DFT calculations, respectively.

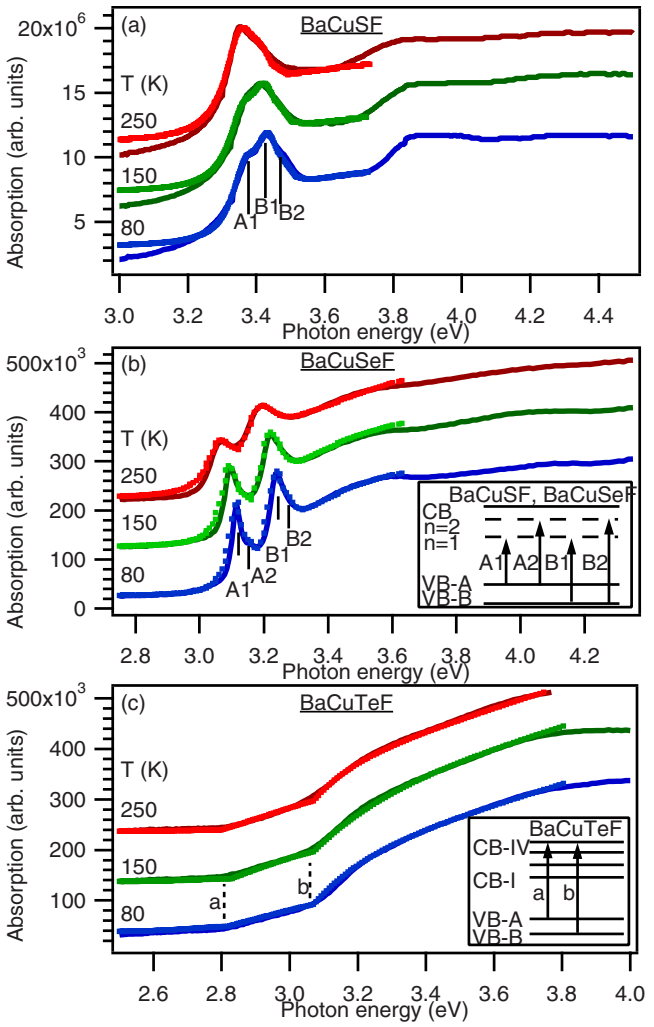

FIG. 3. (Color online) Experimental absorption spectra of (a) BaCuSF, (b) BaCuSeF and (c) BaCuTeF at 80–250 K. The dotted lines are fits based on the analysis described in the text. The spectra are offset on the vertical axis for clarity. Insets: schematic interpretation of the absorption spectra.

theoretical spectra [Fig. 2(c)] because the GGA DFT does not include the electron-hole interaction. Furthermore, the peaks narrow as the temperature is lowered [Figs. 3(a) and 3(b)]. Since the *A*-*B* separation closely matches the calculated spin-orbit splitting, we assign the *A* and *B* absorption peaks to two different excitons, respectively, associated with two spin-orbit split valence bands VB_A and VB_B [Fig. 1(a)]. According to this assignment, the A_1 and B_1 excitonic absorption peaks correspond to creation of the excitons in the ground state ($n=1$), while the high-energy side shoulders A_2 and B_2 observed at low temperatures in BaCuSeF correspond to creation of excitons in the first excited state ($n=2$), where n is a principal quantum number of the hydrogenlike excitonic energy levels.[25] In BaCuSF, absorption shoulder B_2 is also observed, but A_2 almost coincides with B_1 and cannot be resolved. The inset to Fig. 3(b) illustrates the assignment, with the dashed lines meant to represent the many-body exciton in a single-particle picture. We discard the alternative explanation that *A* and *B* represent the ground and excited states of a single exciton because the *A* and *B* peaks have similar intensity. High intensity spin-orbit split excitonic peaks are observed in materials other than BaCu*Ch*F, such as Ba*Ch* (*Ch*=S,Se,Te),[26] MCh_2 (*M*=W,Mo),[27] and LnCuO*Ch* (Ln=La,Pr,Nd).[28]

TABLE III. Experimental optical band gaps and absorption edges in BaCu*Ch*F. Experimental optical band gaps are extracted from fits of Eq. (1) to the data in Fig. 3 using Varshni relationship [Eq. (4)]. Experimental absorption edges are those shown in Fig. 2(a).

Band gap (eV)		BaCuSF	BaCuSeF	BaCuTeF
Absorption edge	Films	3.3	3.1	3.0
	Powders	3.2	3.0	2.3
Optical	E_{gA}	3.47	3.19	2.82
	E_{gB}	3.52	3.31	3.07

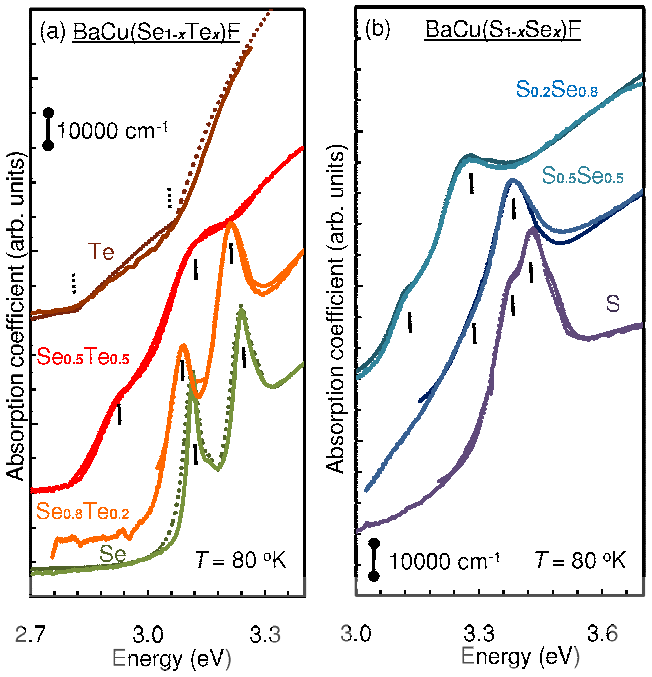

FIG. 4. (Color online) Experimental absorption spectra of (a) $BaCu(Se_{1-x}Te_x)F$ and (b) $BaCu(S_{1-x}Se_x)F$ at 80 K. The dotted lines are fits to the data as discussed in the text. The spectra are offset on the vertical axis for clarity.

The experimental absorption spectra of BaCuSF and BaCuSeF [Figs. 3(a) and 3(b)] are consistent with a 3D Wannier-Mott model, because the intensities of A_2 and B_2 are about 8 times smaller than the intensities of A_1 and B_1, respectively. According to the 3D Wannier-Mott model, the absorption spectrum of a semiconductor with parabolic bands in the presence of electron-hole interaction has the form:[11]

$$\alpha(E) = \sum_i c_i E E_{xi} \times \left[\frac{\pi \exp(z_i)}{\sinh(z_i)} + \sum_{n=1}^{\infty} \frac{4}{n^3} \delta\left(E - E_{gi} + \frac{E_{xi}}{n^2} \right) \right], \quad (1)$$

where c_i is a scaling factor and z_i is an energy variable parameterized by the exciton binding energy E_{xi} and the band gap E_{gi}:

$$z_i = \pi \sqrt{\frac{E_{xi}}{E - E_{gi}}}. \quad (2)$$

The first term in square brackets in Eq. (1) represents band-to-band transitions in the presence of the Coulomb interaction and causes $\alpha(E)$ to increase more rapidly near the band edge than if there were only free carrier absorption. To better fit the data in Figs. 3 and 4, the first term in Eq. (1) was multiplied by a broadening function B_{ci} (E, E_{gi}, Γ_{ci}) similar to that found in literature.[29] The second term in square brackets in Eq. (1) is a sum of delta functions that represent transitions to discrete hydrogenlike excitonic energy levels. Each delta function was approximated in the fits by a Lorentzian L_{xi} $(E - E_{gi} + E_{xi}/n^2, \Gamma_{xi}, w_i)$, where Γ_{xi} is full width at half maximum (FWHM), and $w_i < 1$ is a weighting factor that accounts for the effects of structural disorder and other possible smearing factors on the intensity of the excitonic absorption. Despite the large number of parameters in the model, they are all physically reasonable.

Experimental absorption spectra of BaCu*Ch*F and $BaCu(Ch_{1-x}Ch'_x)F$ are in a good agreement with the 3D Wannier-Mott model as evidenced in Fig. 3 and Fig. 4. A two-dimensional (2D) Wannier-Mott model cannot be fit to experimental data, since the ratio of $n=1$ and $n=2$ excitonic peaks in Fig. 3 is clearly not 27.[11,30] The absorption spectrum in Fig. 3 is consistent with the superposition of two sets of absorption—one from VB_A to CB_I with the associated exciton (A series) and one from VB_B to CB_I with its associated exciton (B series). Thus the B series is superimposed on the continuum absorption from VB_A to CB_I. This structure appears similar to step-functions observed in LaCuO*Ch* thin films.[28] The higher-energy absorption peaks observed in LaCuO*Ch* samples prepared by reactive solid-phase epitaxy (RSPE)[28] are not observed in the *in situ* processed BaCuSF films reported in this work [Fig. 3(a)]. The absence of higher energy peaks in BaCu*Ch*F samples may have to do with a different dimensionality of the excitons, or with better crystallinity of the LaCuO*Ch* films, which are processed at a much higher temperature. We do observe a weak feature in BaCuSF spectrum at 3.8 eV [Fig. 3(a)], which could be a smeared transition from two valence bands to a higher-lying conduction band CB_{II} [Fig. 1(a)]. There is no corresponding feature in BaCuSeF absorption spectrum [Fig. 3(b)] because in this material CB_{II} is almost degenerate with CB_I [Fig. 1(a)].

Experimental and theoretical parameters of the excitons extracted from the 3D Wannier-Mott model are summarized in Table IV. Experimental exciton binding energies E_{xi} were determined from the fit of Eq. (1) to the 80-K absorption spectra in Fig. 3. Next, the corresponding average excitonic radii a_{xi} and reduced effective masses μ_{xi} shown in Table IV were calculated using

$$E_{xi} = \frac{E_H a_H}{\varepsilon} \frac{1}{a_{xi}} = \frac{E_H}{\mu_H \varepsilon^2} \mu_{xi}, \quad (3)$$

where E_H, a_H and μ_H are, respectively, the ionization potential, Bohr radius and reduced mass of the hydrogen atom, and ε is the static relative dielectric constant. Equation (3) was also used to calculate the theoretical binding energies and effective radii of excitons from their theoretical reduced effective masses μ_{xi}, found from the GGA DFT average effective masses of the carriers (Table I). These calculations lead to the conclusion that the high binding energies of the excitons in BaCu*Ch*F (*Ch*=S,Se) result from high out-of-plane effective mass of the holes. The corresponding average effective radius of the excitons is comparable to 1 c axis or 2 a axis lattice constants in BaCu*Ch*F, close to the limit where macroscopic parameters such as ε are meaningful. The dielectric constant of BaCu*Ch*F was approximated by a simple average of those for barium fluoride (ε=7.4), barium sulfate (ε=11.4), and cupric sulfate (ε=10.3).[31] Despite this rough approximation, the theoretical and experimental binding en-

TABLE IV. Parameters of the *A* excitons in BaCu*Ch*F. The exciton binding energy E_x is extracted from the fit of Eq. (1) to the experimental data in Fig. 3. The exciton reduced mass μ_x is calculated from the theoretical data in Table I. The exciton radius a_x and the screening length r_0^{TF} are calculated using Eqs. (3) and (7), respectively.

	BaCuSF		BaCuSeF.		BaCuTeF	
	Experimental	Theoretical	Experimental	Theoretical	Experimental	Theoretical
E_x (meV)	0.095	0.105	0.065	0.087	–	0.171
a_x (nm)	0.87	0.70	1.1	0.85	–	0.43
μ_x (m_e)	0.49	0.90	0.45	0.80	–	1.18
r_0^{TF} (nm)		>1.1		1.1	–	0.20

ergies of the excitons are in fair agreement with each other (Table IV). We note that the macroscopic exciton model is also valid for excitons in Cu_2O, despite their small effective radii.[11]

The FWHM of the excitonic peaks Γ_{xi} and the optical band gaps E_{gi} were extracted from the fits of Eq. (1) to the experimental absorption spectra measured at different temperatures (Fig. 3). In these fits, we constrained the exciton binding energy E_{gi} to that at 80 K, at every experimental temperature. The temperature dependence of Γ_{xi} and E_{gi} is shown in Fig. 5. BaCu*Ch*F optical band gaps decrease with increasing temperature. The temperature dependence of the experimental optical gaps E_{gA} and E_{gB} [Figs. 5(a) and 5(b)] was fit using the Varshni relationship:[32]

$$E_{gi}(T) = E_{gi}(0) - \alpha_i T^2/(T+\beta_i), \tag{4}$$

where α_A=0.19 meV/K and α_B=0.22 meV/K for BaCuSF, α_A=0.36 meV/K and α_B=0.40 meV/K for BaCuSeF, and

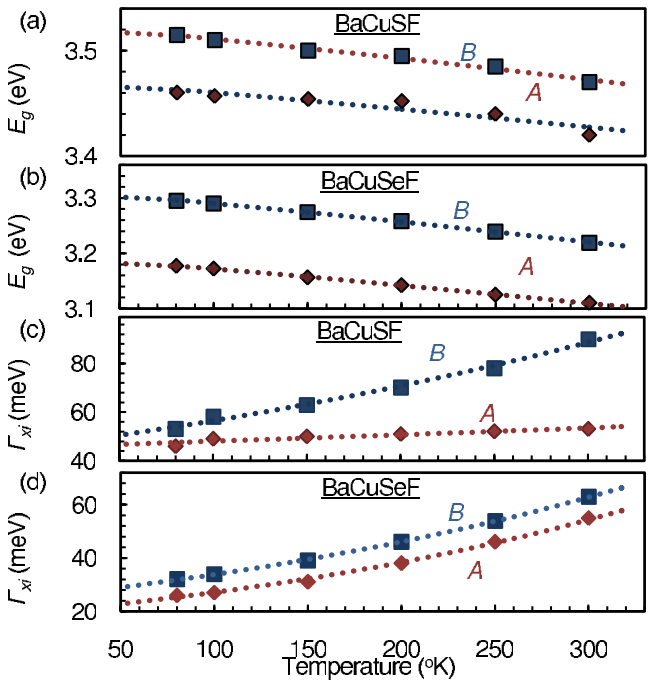

FIG. 5. (Color online) (a and b) Band gaps and (c and d) FWHM of the excitonic peaks in BaCuSF and BaCuSeF absorption spectra for spin-orbit split valence bands *A* and *B*. The dotted lines are fits to the data as discussed in the text.

β_i was set to 100 K for both materials. From these fits we find that zero-temperature experimental optical band gaps of BaCuSF and BaCuSeF $E_{gi}(0)$ (Table III) are in good agreement with theoretical GW predictions (Table II). In Table III, BaCu*Ch*F experimental optical band gaps are also compared to the spectral positions of the optical absorption edges of the BaCu*Ch*F thin films and powders from Fig. 2(b). The experimental optical gaps are higher than the absorption edges [Fig. 2(b)], because of the presence of subgap excitonic absorption peaks in BaCuSF and BaCuSeF thin films. In BaCuSF and BaCuSeF powders, and $BaCu(S_{1-x}Se_x)F$ powder solid solutions studied by our group,[33] the absorption edge determined from the diffuse reflectance measurements by Kubelka-Munk method[34] is 0.1 eV lower than absorption edge of thin films with the same composition, [Fig. 2(b)] possibly due to the disorder and band tail effects of materials prevalent in microcrystalline form.

The excitonic absorption peaks broaden with increasing temperature. The temperature dependence of the FWHM of the excitonic peaks Γ_{xi} [Figs. 5(c) and 5(d)] was fit with an exponential function, since it gave a better fit than a polynomial:

$$\Gamma_{xi}(T) = \Gamma_{xi}(0)\exp(d_i T), \tag{5}$$

where d_A=3.5 mK^{-1} and d_B=3.1 mK^{-1} for BaCuSeF, and d_A=0.54 mK^{-1} and d_B=2.3 mK^{-1} for BaCuSF. The thermal broadening rate of the excitonic peaks in BaCuSF is smaller than in BaCuSeF, because the exciton binding energy in BaCuSF is larger. The FWHM of the peaks in BaCuSF is larger, because the density of native defects in BaCuSF is larger (S is more volatile than Se and can be more easily lost in the pulsed laser deposition process).

Finally, we compare the excitons in BaCuSF, BaCuSeF and other semiconductors. Figure 6 shows an empirical plot of exciton binding energy *vs.* band gap energy for various materials. As examples of 3D-like materials, we present metal pnictides, oxides and chalcogenides, and as examples of 2D-like compounds we show transition-metal dichalcogenides and mixed-anion quaternary compounds. From Fig. 6 we note that: (i) 3D chalcogenides have larger exciton binding energies than 3D pnictides and oxides; (ii) 2D-like materials have larger excitonic binding energy than 3D-like compounds; (iii) the mixed-anion BaCu*Ch*F and LaCuO*Ch* fall on the intersection of the 2D and 3D lines. The effective radius of the excitons in BaCu*Ch*F is comparable to the

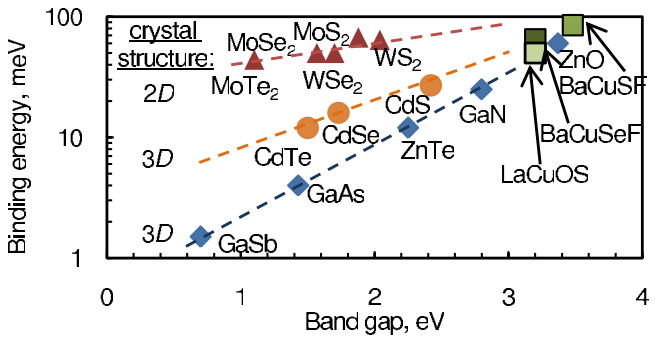

FIG. 6. (Color online) Exciton binding energy as a function of band gap for materials with different crystal structures. Dashed lines are guides for the eye.

c-axis lattice parameter and to twice the *a* axis lattice parameter (Table IV), which makes it difficult to use this size argument to determine the dimensionality of the excitons. At most it might be said that they are close to both 2D and 3D limits, which is consistent with the position of the BaCu*Ch*F points in Fig. 6. In addition we note that 2D-like WSe_2 has excitons that are well described by a 3D Wannier-Mott model,[30] so there is not necessarily a direct correlation between the dimensionality of the crystal structure and dimensionality of the excitons. As discussed in Ref. 30, both the kinetic and potential energy operators in the Hamiltonian must be two dimensional for the excitons to be truly two dimensional. On one hand, the kinetic energy operator is usually two dimensional for layered compounds with anisotropic carrier effective masses. On the other hand, the dimensionality of the potential energy operator depends on the local crystallographic symmetry, which is not always 2D like for layered compounds. Thus the question of the exciton dimensionality in layered materials is quite complicated and requires careful material-specific investigation.

B. BaCuTeF

Two features of experimental absorption spectrum of BaCuTeF require explanation—the large optical band gap of the films (Fig. 2, Tables II and III) and the absence of excitonic absorption even in the highest quality epitaxial samples at the lowest accessible temperatures [Fig. 3(c)].

First, we turn our attention to large optical band gap in the BaCuTeF thin films. According to both GGA DFT and GW, in BaCuTeF the electronic gap is smaller than the optical gap (Table II), so the probability of the lowest energy optical transitions must be small, which can be qualitatively understood as follows. Referring to Fig. 1(b), the VBM is primarily derived from Cu $3d$/Te $5p$ orbitals and the CBM has mainly Ba $5d$/Cu $4s$/Cu $3d$ character. Transitions of the type Cu $3d$−Cu $4s$ or Cu $3d$−Cu $3d$ are suppressed by an electric dipole selection rule ($\Delta l \pm 1$), and transitions of the type Te $5p$−Cu $4s$, Te $5p$−Ba $5d$ and Cu $3d$−Ba $5d$ are suppressed because the initial and final Bloch states have most of their weight on different atoms and the overlap of the corresponding wave functions is small (similar to the Franck-Condon argument in molecular physics). For similar reasons, transitions from VB_A and VB_B to Ba-$5d$-derived CB_{II} and CB_{III} must be also suppressed. In powders, the amount of material is large enough that these weak transitions can be detected, so an absorption edge is at 2.3 eV according to powder diffuse reflectance measurements.[35] In BaCuTeF films, the optical gap is determined by the strong VB-CB_{IV} transition. As schematically shown in the inset of Fig. 3(c), we attribute the two absorption edges α and β to transitions from the spin-orbit split Te $5p$-derived VB_A and VB_B to the Te $5s$-derived CB_{IV}. Corresponding optical band gaps (Table III) are in good agreement with the results of GW calculations (Table II). Similar suppressed lowest energy optical transitions enhance the transparency in the *n* type transparent conductor In_2O_3,[36] and a family of *p*-type transparent conductors $CuMO_2$ (M=Al,Ga,In).[37]

An additional contribution to the extended transparency range of both thin films and powders of BaCuTeF comes from the Moss-Burstein band filling. Band filling can be clearly seen in *n*-type transparent conductors with highly disperse CBs, such as In_2O_3:Sn (Ref. 38) and CdO:In.[39] Since for the wide gap *p*-type BaCuTeF the CB filling is negligible, the shift of the absorption edge may be approximated by the change in the chemical potential in a Fermi-Dirac distribution $f_{FD}(E)$, that can be found using the relationship

$$p = \int_{-\infty}^{0} D_{VB}(E)[1 - f_{FD}(E)]dE, \tag{6}$$

where $D_{VB}(E)$ is the density of states per unit volume, calculated from first principles using GGA DFT and p is the concentration of holes. Experimentally measured $p = 10^{20}$ cm^{-3} in BaCuTeF sets the chemical potential 0.25 eV below the VBM, in reasonable agreement with the 0.19 eV discrepancy between the GW electronic gap (Table II) and energy of the powder absorption edge (Table III). If the concentration of holes in BaCuTeF were 10^{21} cm^{-3}, the Moss-Burstein shift (0.54 eV) would become comparable to the shift caused by suppressed transitions, but the concentration of holes in BaCuTeF is difficult to control, so it is hard to experimentally observe this change.

We turn now to the suppression of excitons in BaCuTeF. The theoretical exciton binding energy in BaCuTeF (Table IV) is much higher than the 7-meV thermal fluctuations that correspond to the lowest accessible temperature of our experimental setup (80 K), but the excitons are absent from the experimental absorption spectra [Fig. 3(c)]. We attribute the lack of excitons in BaCuTeF to screening of the electron-hole interaction by free holes. To explain the absence of the excitonic peaks in BaCuTeF (and their presence in BaCuSF and BaCuSeF), we consider the Thomas-Fermi approximation of the screened electrostatic potential:

$$\varphi(r) = \frac{e}{4\pi\varepsilon_0\varepsilon r}\exp\left(-\frac{r}{r_0^{TF}}\right) = \frac{e}{4\pi\varepsilon_0\varepsilon r}\exp\left(-r\sqrt{\frac{6\pi e^2 p}{\varepsilon\varepsilon_0 E_f}}\right), \tag{7}$$

where e is a unit charge, r is the electron-hole separation, r_0^{TF} is a screening length and E_f is the energy of the charge carriers at the Fermi surface of metal.[40] In the case of a

degenerately doped p-type semiconductor, E_f can be approximated by the average energy of free holes in the valence band:

$$\langle E \rangle = \left[\int_{-\infty}^{0} E D_{VB}(E) f_{FD}(E) dE \right] / \left[\int_{-\infty}^{0} D_{VB}(E) f_{FD}(E) dE \right]. \quad (8)$$

Fermi screening length for three BaCuChF compounds is summarized in Table IV. The concentration of free holes in BaCuTeF is $p=10^{19}-10^{20}$ cm^{-3} at all accessible temperatures, because the conductivity change between from 300 to 80 K is quite small.[41] The resulting screening length of 0.20 nm is smaller than the effective radius of the excitons, so free holes effectively screen the electron-hole interaction and lead to suppression of excitonic absorption in BaCuTeF thin films. In addition, CB_I in BaCuTeF has no Te character [Fig. 1(b)], which precludes creation of the excitons associated with the Te atom. In contrast to BaCuTeF, BaCuSF and BaCuSeF have Ch character in both VB and CB_I, and the screening length in thin films of these materials is larger than the average radius of the excitons due to a lower concentration of free holes.[17]

Since BaCuChF materials were not intentionally doped, free holes must originate from ionized native defects. The local electric fields created by these defects are not sufficient to destroy the excitons in any of three BaCuChF materials. For this calculation, the magnitude of electric field experienced by an electron (or a hole) in the exciton was compared to the electric field at a distance approximately equal to the half of the average distance between the defects. This simple order-of-magnitude estimation was done assuming no defect compensation effects and using an algorithm similar to calculation of metal-insulator transitions in semiconductors.[42]

C. BaCu($Ch_{1-x}Ch'_x$)F solid solutions

The splitting of the peaks in the experimental absorption spectra of the BaCuSF, BaCuSeF and BaCu($S_{1-x}Se_x$)F thin-film solid solutions indicate that the chalcogen atom has a significant influence on the fundamental optical transitions in BaCuChF (Fig. 4), and GGA DFT calculations provide qualitative support [Fig. 1(b)]. As the fraction of the heavy chalcogen x increases in BaCu($Ch_{1-x}Ch'_x$)F thin-film solid solutions, the exciton peaks shift to lower energies due to the decrease of the band gap, which we partially attribute to better overlap of the higher Ch np level with the Cu 3d atomic orbital. Also, the excitonic peaks become less intense with increase of x, due to increased screening of excitons by free carriers. Finally, excitonic peaks in BaCu($Ch_{1-x}Ch'_x$)F are broader than in BaCuChF, because of disorder created by the random filling of the chalcogen sites by Ch and Ch' in thin-film solid solutions.

As shown in Fig. 7(a), the separation of the band gaps E_{gA} and E_{gB}, obtained from the fit of Eq. (3) to the experimental data in Fig. 4, increases with increasing x in the solid solution, reflecting the energy difference between the spin-orbit split valence bands [Fig. 7(a) inset]. Figure 7(b) shows the separation between E_{gA} and E_{gB} as a function of the thin-film solid solution composition. For BaCuChF (Ch=S,Se,Te), experimental separation is larger than the theoretical prediction by about 30 meV, which may be attributed to either imperfections of the thin film samples or to GGA DFT calculation artifacts. Overall, the experimental and theoretical spin-orbit splitting agree better for BaCu($Se_{1-x}Te_x$)F than for BaCu($S_{1-x}Se_x$)F. This is expected,[43] since in BaCu($S_{1-x}Se_x$)F binding energy of the excitons is larger than the spin-orbit splitting [Fig. 7(b), inset].

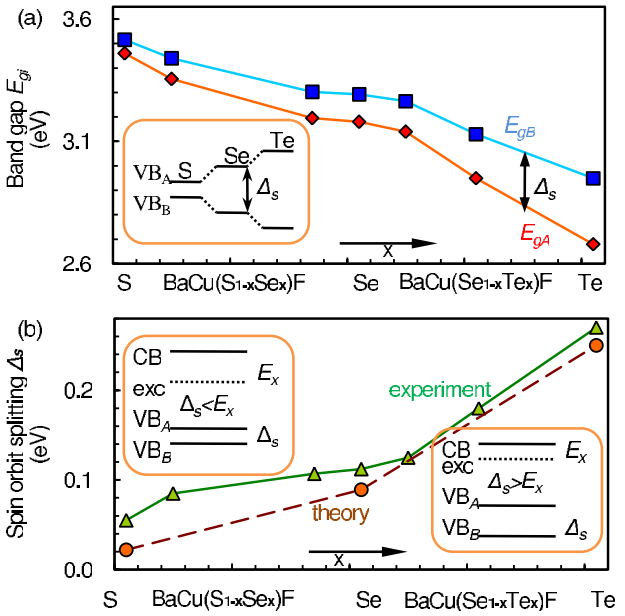

FIG. 7. (Color online) (a) Band gaps and (b) spin-orbit splittings in BaCu($Se_{1-x}Te_x$)F and BaCu($S_{1-x}Se_x$)F. Insets show schematic electronic bands and excitonic levels.

V. SUMMARY

We have built a consistent model that describes the optical properties of BaCuChF (Ch=S,Se,Te) materials based on their absorption spectra and electronic band structure. According to this model, BaCuChF have two series of 3D Wannier-Mott excitons associated with two spin-orbit split valence bands. Spin-orbit splitting increases with increasing atomic weight of a chalcogen in BaCu($Ch_{1-x}Ch'_x$)F. The high-binding energy of the excitons results from the large out-of-plane effective masses of the holes and causes the persistence of excitons above room temperature. In BaCuTeF, the lowest band-to-band transitions are suppressed and the excitons are screened by free holes.

ACKNOWLEDGMENT

This work was supported by NSF (Grant No. DMR 0804916).

*andriy.zakutayev@lifetime.oregonstate.edu
†Corresponding author. tate@physics.oregonstate.edu

[1] K. Ueda, S. Inoue, S. Hirose, H. Kawazoe, and H. Hosono, Appl. Phys. Lett. **77**, 2701 (2000).
[2] H. Yanagi, J. Tate, S. Park, C.-H. Park, and D. A. Keszler, Appl. Phys. Lett. **82**, 2814 (2003).
[3] Y. Kamihara, H. Hiramatsu, M. Hirano, R. Kawamura, H. Yanagi, T. Kamiya, and H. Hosono, J. Am. Chem. Soc. **128**, 10012 (2006).
[4] H. Hiramatsu, K. Ueda, H. Ohta, M. Hirano, M. Kikuchi, H. Yanagi, T. Kamiya, and H. Hosono, Appl. Phys. Lett. **91**, 012104 (2007).
[5] H. Yanagi, S. Ohno, T. Kamiya, H. Hiramatsu, M. Hirano, and H. Hosono, J. Appl. Phys. **100**, 033717 (2006).
[6] Y. Kamihara, T. Watanabe, M. Hirano, and H. Hosono, J. Am. Chem. Soc. **130**, 3296 (2008).
[7] J. F. Wager, D. A. Keszler, and R. E. Presley, *Transparent Electronics* (Springer, Berlin, 2008).
[8] M. Yasukawa, K. Ueda, and H. Hosono, J. Appl. Phys. **95**, 3594 (2004).
[9] H. Hiramatsu, K. Ueda, H. Ohta, T. Kamiya, and M. Hirano, Appl. Phys. Lett. **87**, 211107 (2005).
[10] J. A. Spies, R. Schafer, J. F. Wager, P. Hersh, H. A. S. Platt, D. A. Keszler, G. Schneider, R. Kykyneshi, J. Tate, X. Liu, A. D. Compaan, and W. N. Shafarman, Sol. Energy Mater. Sol. Cells **93**, 1296 (2009).
[11] N. Peyghambarian, S. W. Koch, and A. Mysorowicz, *Introduction to Semiconductor Optics* (Prentice Hall, Englewood Cliffs, NJ, 1993).
[12] K. Ueda, H. Hiramatsu, M. Hirano, T. Kamiya, and H. Hosono, Thin Solid Films **496**, 8 (2006).
[13] K. Ueda, S. Inoue, H. Hosono, N. Sarukura, and M. Hirano, Appl. Phys. Lett. **78**, 2333 (2001).
[14] T. Kamiya, K. Ueda, H. Hiramatsu, H. Kamioka, H. Ohta, M. Hirano, and H. Hosono, Thin Solid Films **486**, 98 (2005).
[15] H. Hiramatsu, K. Ueda, K. Takafuji, H. Ohta, M. Hirano, T. Kamiya, and H. Hosono, J. Appl. Phys. **94**, 5805 (2003).
[16] K. Ueda, H. Hosono, and N. Hamada, J. Phys.: Condens. Matter **16**, 5179 (2004).
[17] J. Tate, P. F. Newhouse, R. Kykyneshi, P. A. Hersh, J. Kinney, D. H. McIntyre, and D. A. Keszler, Thin Solid Films **516**, 5795 (2008).
[18] A. Zakutayev, D. H. McIntyre, G. Schneider, D. A. Keszler, C.-H. Park, and J. Tate, Thin Solid Films (to be published 2010).
[19] Y. Hishikawa, N. Nakamura, S. Tsuda, S. Nakano, Y. Kishi, and Y. Kuwano, Jpn. J. Appl. Phys. **30**, 1008 (1991).
[20] P. Blaha, K. Schwarz, G. Madsen, D. Kvasnicka, and J. Luitz, *WIEN2k, An Augmented Plane* Wave+Local *Orbitals Program for Calculating Crystal Properties* (Karlheinz Schwarz, Techn. Universität Wien, Austria, 2001).
[21] M. Weinert, G. Schneider, R. Podloucky, and J. Redinger, J. Phys.: Condens. Matter **21**, 084201 (2009).
[22] M. Shishkin and G. Kresse, Phys. Rev. B **75**, 235102 (2007).
[23] G. Kresse and J. Furthmüller, Phys. Rev. B **54**, 11169 (1996).
[24] H. Yanagi, J. Tate, S. Park, C.-H. Park, D. A. Keszler, M. Hirano, and H. Hosono, J. Appl. Phys. **100**, 083705 (2006).
[25] J. I. Pankove, *Optical Processes in Semiconductors* (Courier Dover Publications, Mineola, NY, 1975).
[26] R. J. Zollweg, Phys. Rev. **111**, 113 (1958).
[27] A. R. Beal, J. C. Knights, and W. Y. Liang, J. Phys. C **5**, 3531 (1972).
[28] K. Ueda, H. Hiramatsu, H. Ohta, M. Hirano, T. Kamiya, and H. Hosono, Phys. Rev. B **69**, 155305 (2004).
[29] J. F. Muth, R. M. Kolbas, A. K. Sharma, S. Oktyabrsky, and J. Narayan, J. Appl. Phys. **85**, 7884 (1999).
[30] A. R. Beal and W. Y. Liang, J. Phys. C **9**, 2459 (1976).
[31] http://www.asiinstr.com/technical/dielectric%20constants.htm.
[32] Y. P. Varshni, Physica **34**, 149 (1967).
[33] C.-H. Park, D. A. Keszler, H. Yanagi, and J. Tate, Thin Solid Films **445**, 288 (2003).
[34] S. Shionoya and W. M. Yen, *Phosphor Hanbook* (CRC Press, Boca Raton, FL, 1998).
[35] C.-H. Park, R. Kykyneshi, A. Yokochi, J. Tate, and D. A. Keszler, J. Solid State Chem. **180**, 1672 (2007).
[36] A. Walsh, J. L. F. Da Silva, S.-H. Wei, C. Korber, A. Klein, L. F. J. Piper, A. DeMasi, K. E. Smith, G. Panaccione, P. Torelli, D. J. Payne, A. Bourlange, and R. G. Egdell, Phys. Rev. Lett. **100**, 167402 (2008).
[37] X. Nie, S.-H. Wei, and S. B. Zhang, Phys. Rev. Lett. **88**, 066405 (2002).
[38] P. F. Newhouse, C.-H. Park, D. A. Keszler, J. Tate, and P. S. Nyholm, Appl. Phys. Lett. **87**, 112108 (2005).
[39] N. Ueda, H. Maeda, H. Hosono, and H. Kawazoe, J. Appl. Phys. **84**, 6174 (1998).
[40] N. W. Ashcroft and N. D. Mermin, *Solid State Physics* (Holt, Rinehart, and Winston, New York, 1976).
[41] R. Kykyneshi, D. H. McIntyre, J. Tate, C.-H. Park, and D. A. Keszler, Solid State Sci. **10**, 921 (2008).
[42] M. P. Marder, *Condensed Matter Physics* (John Wiley, New York, 2000).
[43] Y. Zhang, G. M. Dalpian, B. Fluegel, S.-H. Wei, A. Mascarenhas, X.-Y. Huang, J. Li, and L.-W. Wang, Phys. Rev. Lett. **96**, 026405 (2006).